INTERPRETABLE MULTIPLE LOSS FUNCTIONS IN A LOW-RANK DEEP IMAGE PRIOR BASED METHOD FOR SINGLE HYPERSPECTRAL IMAGE SUPER-RESOLUTION

Tatiana Gelvez[1] *Jorge Bacca*[2] *Henry Arguello*[2]

[1]Department of Electrical Engineering, Universidad Industrial de Santander, Bucaramanga, Colombia
[2]Department of Computer Science, Universidad Industrial de Santander, Bucaramanga, Colombia

ABSTRACT

This paper presents a single hyperspectral image super-resolution (HSI-SR) method based on the non data-driven deep image prior approach, where the prior information of the image is intrinsically learned through the weights and the structure of a neural network. Precisely, we propose a scheme composed of a sequence of independent and interpretable deep-blocks, whose outputs are affected in the back-propagation step not only by the general loss-function, but also by a single loss-function, resulting in a scheme using multiple loss-functions. The internal architecture of each deep-block consists of a low-rank decomposition with two block-layers inspired by the linear mixture model, where the spectral image is formed as the product between an abundance and an endmember matrix, such that, the features of the first block-layer and the weights of the second block-layer can be interpreted as the abundances and the endmembers, respectively. In the experimental section, we showed the remarkable performance of the proposed HSI-SR method concerning the extensive reviewed state-of-the-art approaches.

***Index Terms*—** Neural networks, Deep image prior, Low-rank approximation, Hyperspectral image super-resolution.

1. INTRODUCTION

Single hyperspectral image super-resolution (HSI-SR) recovery technique addresses the spatial-spectral tradeoff of current optical devices, that acquire a limited amount of incident energy when sensing HSIs with dozens or hundreds of narrow spectral bands, sacrificing spatial resolution. For this, HSI-SR methods aim to infer a high-spatial-resolution HSI (HR-HSI) from the acquired low-spatial-resolution HSI (LR-HSI) with no additional auxiliary images by exploiting the high spatial-spectral correlations as prior information. Model-based optimization methods incorporate such prior information through hand-crafted regularizers as total-variation [1], sparse representation [2], and low-rankness [3]. In contrast, deep learning (DL)-based methods learn the prior information or the entire decoder operator to model the relationship between the LR-HSI and the HR-HSI through the training of a huge amount of datasets [4, 5]. For instance, authors in [6, 7, 8] introduce convolutional neural networks (CNNs) based on 3D filters to better exploit the spatial-spectral correlations. Still, DL-based methods can become impractical given the high cost of acquiring several HSI training datasets [9, 10]. The recent so-called deep image prior (DIP) approach showed that the prior information can be embodied in the weights of the neural network allowing to solve various inverse problems, such as HSI-SR, in a non data-driven manner [11]. For instance, [12] integrated DIP with 3D convolutions containing higher low-level image information, [13] boosted DIP strategy by adding explicit regularization, and [14] provided an evolutionary strategy to automatically search for the optimal hyper-parameters of the DIP architecture.

Previous DIP-based methods for HSI-SR commonly employ a standard loss-function of the output of the model. Contrary, we propose a DIP-based HSI-SR method that incorporates the idea of using multiple loss-functions associated with multiple deep-blocks forming the deep architecture. This multiple deep-blocks scheme considers that the deeper the network, the finer the learned features estimating the spatial-spectral correlations of HSIs. Besides, we propose each deep-block to be interpretable in the sense that its internal structure consists of two block-layers inspired by the linear mixture model (LMM), where the outputs can be interpreted as a low-rank approximation of the HR-HSI, decomposed as a matrix product between, an endmember matrix containing the spectral response of few independent materials in the scene, and an abundance matrix including the fractional proportions of the endmembers at each spatial location [15]. The proposal then recovers the HR-HSI from the LR-HSI in a non data-driven manner by including the prior information on the architecture, where neither the abundances nor the endmembers are known. Instead, at each deep-block, the features of the first block-layer can be interpreted as the abundances, and the weights of the second block-layer as the endmembers, where some included regularizers consider the LMM constraints.

Simulations over datasets showed the effectiveness of the proposed interpretable architecture for HSI-SR, even when compared against data-driven methods. In particular, the improvement is obtained when using the sum of the single loss-functions affecting the multiple deep-blocks, and the intrinsic regularization by the neural network architecture.

2. THEORETICAL BACKGROUND

2.1. Single Hyperspectral Image Super-resolution

Let $\mathbf{f} \in \mathbb{R}^{N_h^2 L}$ denote the vector form of an HR-HSI with $(N_h \times N_h)$ spatial pixels and L spectral bands. The LR-HSI acquisition is given by the following forward linear model

$$\mathbf{f}_{low} = \mathbf{DBf}+\boldsymbol{\eta}, \tag{1}$$

where $\mathbf{f}_{low} \in \mathbb{R}^{N_l^2 L}$ stands for the observed LR-HSI, with $N_l \times N_l$ spatial pixels, and L spectral bands; $\mathbf{D} \in \mathbb{R}^{N_l^2 L \times N_h^2 L}$ denotes a spatial downsampling operator, where $N_l = (1/d)N_h$, with $d \in \mathbb{Z}_+$ being a downsampling factor; $\mathbf{B} \in \mathbb{R}^{N_h^2 L \times N_h^2 L}$ denotes a spatial blurring operator, and $\boldsymbol{\eta} \in \mathbb{R}^{N_l^2 L}$ stands for added additive Gaussian noise.

2.2. Linear Mixture Model for Hyperspectral Images

The linear mixture model (LMM) states that natural scenes contain a few number $r \ll L$ of materials defined uniquely by its spectral response. Then, the i^{th} spatial pixel $\mathbf{f}_i \in \mathbb{R}^L$ can be modeled as $\mathbf{f}_i = \mathbf{E}\mathbf{a}_i$, where $\mathbf{E} \in \mathbb{R}^{L\times r}$ is an endmember matrix, whose columns contain a unique spectral response, and $\mathbf{a}_i \in \mathbb{R}^r$ is an abundance vector, containing the fractional proportions of each endmember at the i^{th} spatial pixel, for $i = 1, \ldots, N_h^2$. Then, $\mathbf{f}$ can be low-rank decomposed as

$$\mathbf{f} = (\mathbf{E} \otimes \mathbf{I}_{N_h^2})\bar{\mathbf{a}} = \bar{\mathbf{E}}\bar{\mathbf{a}}, \tag{2}$$

where $\bar{\mathbf{a}} \in \mathbb{R}_+^{N_h^2 r} = [\mathbf{a}_1^T \ \ldots \ \mathbf{a}_i^T \ \ldots \ \mathbf{a}_{N_h^2}^T]^T$ stacks the abundances; $\bar{\mathbf{E}} \in \mathbb{R}_+^{N_h^2 L \times N_h^2 r}$ encompasses the endmembers; $\mathbf{I}_{N_h^2}$ refers to an identity matrix of size N_h^2; and $\otimes$ denotes the Kronecker product, introduced to apply the endmembers along the spatial pixels, maintaining a vector notation.

The LMM entails the physical constraints that a mixed pixel has an entire composition, such that, the sum of non-negative fractional proportions must be one, i.e. $\mathbf{a}_i[a] \geq 0$, and $\sum_{a=1}^r \mathbf{a}_i[a] = 1, \forall i$. Also, since the endmembers connote light intensities they are non-negative [16].

3. PROPOSED SINGLE HYPERSPECTRAL SUPER-RESOLUTION METHOD

The proposed idea is to find a deep model based on the low-rank decomposition $\bar{\mathbf{E}}\bar{\mathbf{a}}$, such that, a super-resolved image can be estimated. Then, the proposed HSI-SR scheme solves the following optimization problem based on the DIP approach that considers the image prior information implicitly through fitting the weights of a deep model given by

$$\hat{\theta} \in \underset{\theta}{\operatorname{argmin}} \ \left\|\mathbf{f}_{low} - \mathbf{DB}\mathcal{M}_\theta(\mathbf{f}^0)\right\|_2^2, \tag{3}$$

where $\hat{\mathbf{f}} := \mathcal{M}_{\hat{\theta}}(\mathbf{f}^0)$ denotes the estimated HR-HSI, $\mathbf{f}^0 \in \mathbb{R}^{N_h^2 L}$ denotes a bicubic interpolation taken from $\mathbf{f}_{low}$, given as the input of the deep generator model $\mathcal{M}_\theta(\cdot) : \mathbb{R}^{N_h^2 L} \to \mathbb{R}^{N_h^2 L}$, with θ as the adjustable deep parameters. Notice that, although problem in (3) is based on a deep model, it only requires the LR-HSI, $\mathbf{f}_{low}$, and the forward operators $\mathbf{DB}$, i.e, it is non data-driven. Precisely, we aim to capture the prior information implicitly by proposing an adequate design of the deep generative model, $\mathcal{M}_\theta(\cdot)$. For this, we determine the architecture of the deep generative model to be composed by a sequence of multiple interpretable deep-blocks, containing two block-layers inspired by the LMM, so that, the k^{th} deep-block can be mathematically expressed as

$$\mathcal{M}_{\theta^k}(\mathbf{f}^{k-1}) = \mathbf{f}^k = \mathcal{E}_{\mathbf{E}^k}(\mathcal{A}_\theta^k(\mathbf{f}^{k-1})), \tag{4}$$

where $\mathcal{A}_\theta^k(\cdot) : \mathbb{R}^{N_h^2 L} \to \mathbb{R}^{N_h^2 r}$ models the first block-layer, referred to as the abundance block-layer, consisting of a CNN that receives and properly filters the input to obtain an output whose properties and dimensions should match for being interpreted as the abundances. $\mathcal{E}_{\mathbf{E}^k}(\cdot) : \mathbb{R}^{N_h^2 r} \to \mathbb{R}^{N_h^2 L}$ models the fully connected second block-layer, referred to as the endmember block-layer, consisting of an operator that performs the matrix multiplication between the learned features in the abundance block-layer $\bar{\mathbf{a}}$, and the adjusted weights in the endmember block-layer $\mathbf{E}$, whose dimensions should match to be interpreted as the endmembers according to the LMM in (2).

Then, the proposed deep model can be expressed as

$$\mathcal{M}_\theta(\mathbf{f}^0) = \hat{\mathbf{f}} = \mathcal{M}_{\theta^K}(\mathcal{M}_{\theta^{K-1}}(\cdots \mathcal{M}_{\theta^1}(\mathbf{f}^0))), \tag{5}$$

where $\boldsymbol{\theta} = [\boldsymbol{\theta}^1, \ldots, \boldsymbol{\theta}^k, \ldots \boldsymbol{\theta}^K]$ stacks the adjustable weights of each deep-block, $\mathbf{f}^k := \mathcal{M}_{\theta^k}(\mathbf{f}^{k-1})$, with each $\mathbf{f}^k$ using a single loss-function as detailed in following sub-sections.

3.1. Abundance Block-layer

The abundance block-layer involves a CNN that filters and operates the spatial dimension of the previous deep-block output. This, given that the abundances entail the spatial correlations of the underlying HSI. Mathematically, the output of the abundance block-layer at the k^{th} deep-block, interpreted as the estimated abundances $\bar{\mathbf{a}}^k \in \mathbb{R}^{N_h^2 r}$ can be expressed as

$$\bar{\mathbf{a}}^k = \mathcal{A}_{\theta^k}(\mathbf{f}^{k-1}). \tag{6}$$

Notice that r denotes a tunable hyper-parameter related to the amount of endmembers present in the scene. The abundance block-layer is based on an autoencoder network, with six 2D convolutional layers with kernel sizes of 3×3, where the number of features increases symmetrically from L to $3L$, and then decreases to L. A value of $L = 32$ was chosen for this work, where the spatial dimensions are preserved using a padding strategy. The abundance block-layer also adds the LMM physical constraints described in Section 2.2 by using the *sigmoid* function as the activation of the network output $\bar{\mathbf{a}}^k$, and including an explicit regularization term in the loss-function, $R(\bar{\mathbf{a}}^k) = \sum_{a=1}^r \mathbf{a}_i^k[a] = 1$, with $\mathbf{a}_i[a] \geq 0, \forall i$.

3.2. Endmember Block-layer

The endmember block-layer consists of a trainable layer that follows the LMM to adjust the underlying spectral responses by performing a matrix multiplication between the output of the previous abundance block-layer $\bar{\mathbf{a}}^k$, and the learned weights, in such a manner that these weights can be interpreted as the estimated endmembers at the k^{th} deep-block. Mathematically, the endmember block-layer is expressed as

$$\mathbf{f}^k = \mathcal{E}_{\mathbf{E}^k}\left(\bar{\mathbf{a}}^k\right) = (\mathbf{E}^k \otimes \mathbf{I}_{N_h^2})\bar{\mathbf{a}}^k, \tag{7}$$

This block-layer also includes the non-negative constraint described in Section 2.2 by projecting the estimated endmembers into $\mathbb{R}_+$ at each gradient step.

3.3. Multiple Loss-functions

In (3) the DIP-based approach applies the forward operators $\mathbf{DB}$ at the output of the deep model to estimate the LR-HSI. Then, the proposal employs such forward operators at the output of each one of the multiple deep-blocks. Furthermore, we propose adjusting each internal architecture weights to refine the learned estimation as the block is deeper by minimizing a single loss-function containing the loss from the difference between the observed LR-HSI and the predicted LR-HSI of each deep-block and the LMM physical constraints. The proposal then solves the optimization problem given by

$$\{\boldsymbol{\theta}^*\} \in \arg\min_{\boldsymbol{\theta}} \sum_k \tau_k \mathcal{L}^k\left(\mathcal{M}_{\theta^k}(\mathbf{f}^{k-1})|\ \mathbf{f}_{low}, \mathbf{DB}\right), \tag{8}$$

$$\mathcal{L}^k(\mathbf{f}^k|\ \mathbf{f}_{low}, \mathbf{DB}) = \left\|\mathbf{f}_{low} - \mathbf{DB}\mathbf{f}^k\right\|_2^2 + \gamma^k \sum_{a=1}^{r} \mathbf{a}_i^k[a] = 1,$$

where, $\tau_k > 0$ index the weights of the single loss-function of each deep-block, and $\gamma_k > 0$ denote the regularization parameters that control the trade-off between the fidelity-data and the abundance constraint. The output at each deep-block can be interpreted as the estimated HR-HSI; nonetheless, the average between the outputs of the last two deep-blocks were chosen as the estimated HR-HSI to better consider the learned features in the final estimations as, $\hat{\mathbf{f}} = (\mathbf{f}^K + \mathbf{f}^{K-1})/2$.

Figure 1 outlines our DIP-based HSI-SR method, where the HR-HSI is estimated trough multiple interpretable deep-blocks inspired by the LMM with two block-layers, each one referring to the abundance and endmembers, respectively.

4. SIMULATIONS AND RESULTS

The conducted experiments employ two public available datasets, the hyperspectral Pavia Center[1], and the Stuff_toys image taken from the spectral CAVE dataset [17] for two downsampling factors, $d = 4$ and $d = 8$. The Pavia Center

[1] Available in http://www.ehu.eus/ccwintco/. Accessed: 17-Feb-2021.

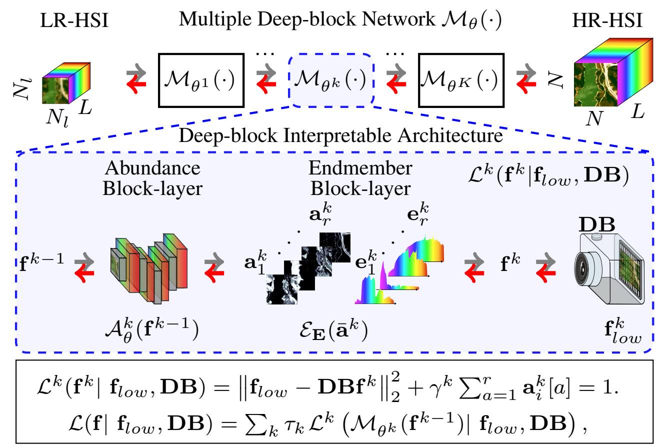

Fig. 1: Proposed DIP-based single HSI-SR method. A bicubic interpolation of the LR-HSI is used as the input $\mathbf{f}_0$ of a sequence of deep-blocks shown at the top. The zoomed version of the k^{th} deep-block depicted at the bottom, where the architecture is composed of the abundance block-layer, consisting in a CNN, and the endmember block-layer performing the matrix product according to the LMM. Finally, the general loss-function considers the sum of the single losses employed by the multiple deep-blocks.

was acquired with the ROSIS sensor in 2001. It contains 102 spectral bands and 1096×1096 spatial pixels, where the water vapor absorption and noisy spectral bands were removed from the original 115 observed spectral bands. We used one sub-region of 224×224 spatial pixels for testing in concordance to experiments in [6]. The CAVE dataset consists of 32 spectral images with 512×512 spatial pixels, and 31 spectral bands ranging from 400nm to 700nm at 10nm steps.

The performance of the proposal was compared against several state-of-the-art methods, including the bicubic interpolation; four deep sinlge gray/RGB image SR methods, EDSR [18], RCAN [19], and SAN [20]; four data-driven DL-based single HSI-SR methods, 3DCNN [8], GDRRN [21], and SSPSR [6]; and a non data-driven, DL-based method, DIP [12]. Remark that the proposed method follows a non data-driven framework. The optimization was solved using the the Adam algorithm [22] with a learning rate of $1e^{-3}$, all hyper-parameters γ^k set to 0.5, and a different value for the rank, r in (6), and number of deep-blocks, K, for each dataset through cross-validation. Precisely, we established $r = 6$ and $K = 3$, and $r = 12$ and $K = 4$, for Pavia Center and Stuff_toys, respectively. All experiments were run on an Intel Xeon W-3223, 64GB of memory, and a NVIDIA RTX 3090 GPU with 24GB of memory[2].

The quality improvement is quantified through the spectral angle mapper (SAM), the root mean squared error (RMSE), the dimensionless global relative error of synthesis (ERGAS), the peak signal-to-noise ratio (PSNR), and the

[2] The source code is publicly available in `https://github.com/TatianaGelvez/Interpretable_HSI_SR`

structural similarity (SSIM) metrics calculated as in [23, 24].

Tables 1 and 2 compare the quantitative results for the single HSI-SR along the evaluated methods for the Pavia Center and Stuff_toys datasets, respectively. There, it can be seen that our proposed non data-driven method outperforms or achieves competitive quality even against the data-driven methods such as the SSPSR for both datasets, both downsampling factors, and all evaluated metrics. Further, we remark that the obtained spectral quality measured with the SAM metric results particularly improved for the hyperspectral Pavia Center dataset. This, because of the low-rank prior can be better exploited when there is a high number of spectral bands that cause higher spectral correlations, which are taken into account within our interpretable deep-blocks. In order to see the additional advange of the proposed inspired network, Fig. 2 depicts the obtained adjusted weights of the second block-layer $\mathbf{E}$, and the features of the first block-layer $\bar{\mathbf{a}}$. There, it can be observed that such outputs can effectively be interpreted as a set of endmembers and abundances, what becomes in additional information that can be useful for further high-level applications. Finally, Fig. 3 shows a visual comparison of the RGB mapping of some super-resolved images for the Pavia dataset, where the proposed method shows a better spatial quality, particularly for high down-sampling factors.

Table 1: Quantitative Results for the Pavia Center Dataset

Method	d	SAM↓	RMSE↓	ERGAS↓	PSNR↑	SSIM ↑
Bicubic	4	6.1399	0.0437	6.8814	27.5874	0.6961
EDSR	4	5.8657	0.0379	6.0199	28.7981	0.7722
RCAN	4	5.9785	0.0376	6.0485	28.8165	0.7719
SAN	4	5.9590	0.0374	5.9903	28.8554	0.7740
3DCNN	4	5.8669	0.0396	6.2665	28.4114	0.7501
GDRRN	4	5.4750	0.0393	6.2264	28.4726	0.7530
SSPSR	4	5.4612	0.0362	**5.8014**	29.1581	0.7903
DIP	4	6.2665	0.0410	6.4845	28.1061	0.7365
Proposed	4	**4.2120**	**0.0352**	5.8084	**29.914**	**0.8396**
Bicubic	8	7.8478	0.0630	4.8280	24.5972	0.4725
EDSR	8	7.8594	0.05983	4.6359	25.0041	0.5130
RCAN	8	7.9992	0.0604	4.6930	24.9183	0.5086
SAN	8	8.0371	0.0609	4.7646	24.8485	0.5054
3DCNN	8	7.6878	0.0605	4.6469	24.9336	0.5038
GDRRN	8	7.3531	0.0607	4.6220	24.8648	0.5014
SSPSR	8	7.3312	0.0586	4.5266	25.1985	0.5365
DIP	8	7.9281	0.0618	4.7366	24.7252	0.4963
Proposed	8	**6.7855**	**0.0485**	**4.0015**	**26.9041**	**0.7148**

Table 2: Quantitative Results for the Stuff_toys Dataset

Method	d	SAM↓	RMSE↓	ERGAS↓	PSNR↑	SSIM ↑
Bicubic	4	4.1759	0.0212	5.2719	34.7214	0.9277
EDSR	4	3.5499	0.0149	3.5921	38.1575	0.9522
RCAN	4	3.6050	0.0142	3.4178	38.7585	0.9530
SAN	4	3.5951	0.0143	3.4200	38.7188	0.9531
3DCNN	4	3.3463	0.0154	3.7042	37.9759	0.9522
GDRRN	4	3.4143	0.0145	3.5086	38.4507	0.9538
SSPSR	4	**3.1846**	0.0138	3.3384	39.0892	0.9553
DIP	4	8.4935	0.0124	2.5358	38.1329	0.9631
Proposed	4	5.3285	**0.0110**	**2.1997**	**39.1640**	**0.9821**
Bicubic	8	5.8962	0.0346	4.2175	30.2056	0.8526
EDSR	8	5.6865	0.0279	3.3903	32.4072	0.8842
RCAN	8	5.9771	0.0268	3.1781	32.9544	0.8884
SAN	8	5.8683	0.0267	3.1437	33.0012	0.8888
3DCNN	8	5.0948	0.0292	3.5536	31.9691	0.8863
GDRRN	8	5.3597	0.0280	3.3460	32.5763	0.8890
SSPSR	8	**4.4874**	0.0257	3.0419	33.4340	0.9010
DIP	8	8.3342	0.0231	2.3697	32.7324	0.9291
Proposed	8	5.5027	**0.0208**	**2.1061**	**33.6270**	**0.9432**

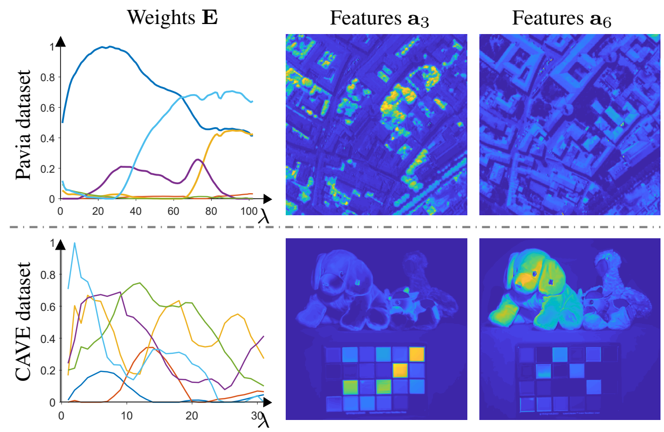

Fig. 2: Visualization of some learned features and adjusted weights for $d = 4$. The output of each deep-block can be effectively interpreted as the endmembers $\mathbf{E}$ and the abundances $\bar{\mathbf{a}}$.

5. CONCLUSIONS

This paper presented a single HSI-SR method based on the non data-driven DIP approach, where the proposed deep generative model is composed of multiple interpretable deep-blocks. The internal architecture is further inspired by the low-rank decomposition given by the LMM, such that, the first block-layer involves a CNN whose output dimensions match the abundances, and the second block-layer involves a matrix product whose adjusted weights match the endmembers. In addition, the general loss-function is composed by the sum of multiple single losses affecting independently each deep-block. The experiments showed that the proposal outperforms state-of-the-art methods, even those data-driven. A better performance was evidenced in images with many spectral bands, where the low-rankness can be fully exploited.

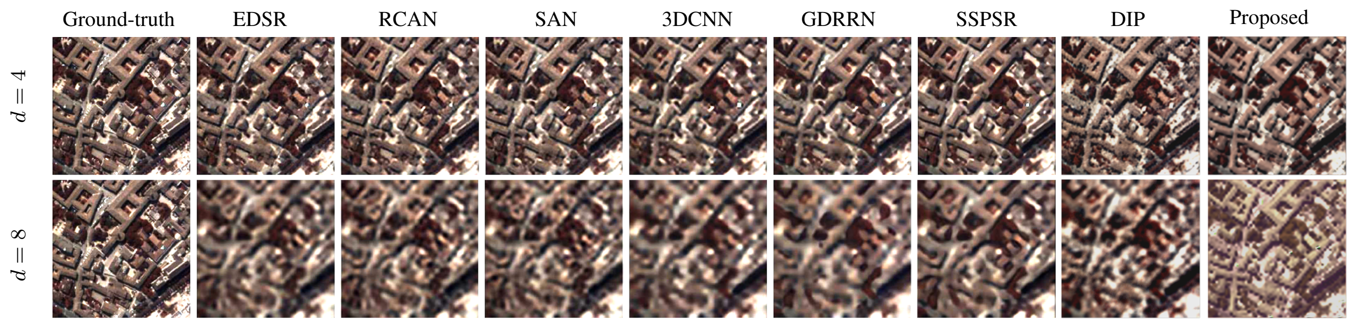

Fig. 3: RGB representation of the reconstructed composite images of Pavia datatest with upsampling factor $d = 4$ (*top*) and $d = 8$ (*bottom*). Notice that, the spatial quality is especially improved for a factor $d = 8$.

6. REFERENCES

[1] Yao Wang, Xi'ai Chen, Zhi Han, Shiying He, et al., "Hyperspectral image super-resolution via nonlocal low-rank tensor approximation and total variation regularization," *Remote Sensing*, vol. 9, no. 12, pp. 1286, 2017.

[2] Yang Xu, Zebin Wu, Jocelyn Chanussot, and Zhihui Wei, "Nonlocal patch tensor sparse representation for hyperspectral image super-resolution," *IEEE Transactions on Image Processing*, vol. 28, no. 6, pp. 3034–3047, 2019.

[3] Jorge Bacca, Claudia V Correa, and Henry Arguello, "Noniterative hyperspectral image reconstruction from compressive fused measurements," *IEEE Journal of Selected Topics in Applied Earth Observations and Remote Sensing*, vol. 12, no. 4, pp. 1231–1239, 2019.

[4] Qiang Li, Qi Wang, and Xuelong Li, "Mixed 2d/3d convolutional network for hyperspectral image super-resolution," *Remote Sensing*, vol. 12, no. 10, pp. 1660, 2020.

[5] Yuan Yuan, Xiangtao Zheng, and Xiaoqiang Lu, "Hyperspectral image superresolution by transfer learning," *IEEE Journal of Selected Topics in Applied Earth Observations and Remote Sensing*, vol. 10, no. 5, pp. 1963–1974, 2017.

[6] Junjun Jiang, He Sun, Xianming Liu, and Jiayi Ma, "Learning spatial-spectral prior for super-resolution of hyperspectral imagery," *IEEE Transactions on Computational Imaging*, vol. 6, pp. 1082–1096, 2020.

[7] Yong Li, Lei Zhang, Chen Dingl, Wei Wei, and Yanning Zhang, "Single hyperspectral image super-resolution with grouped deep recursive residual network," in *2018 IEEE Fourth International Conference on Multimedia Big Data (BigMM)*. IEEE, 2018, pp. 1–4.

[8] Shaohui Mei, Xin Yuan, Jingyu Ji, Yifan Zhang, Shuai Wan, and Qian Du, "Hyperspectral image spatial super-resolution via 3d full convolutional neural network," *Remote Sensing*, vol. 9, no. 11, pp. 1139, 2017.

[9] Gregory Ongie, Ajil Jalal, Christopher A Metzler Richard G Baraniuk, Alexandros G Dimakis, and Rebecca Willett, "Deep learning techniques for inverse problems in imaging," *IEEE Journal on Selected Areas in Information Theory*, 2020.

[10] Lizhi Wang, Tao Zhang, Ying Fu, and Hua Huang, "Hyperreconnet: Joint coded aperture optimization and image reconstruction for compressive hyperspectral imaging," *IEEE Transactions on Image Processing*, vol. 28, no. 5, pp. 2257–2270, 2018.

[11] Dmitry Ulyanov, Andrea Vedaldi, and Victor Lempitsky, "Deep image prior," in *Proceedings of the IEEE Conference on Computer Vision and Pattern Recognition*, 2018, pp. 9446–9454.

[12] Oleksii Sidorov and Jon Yngve Hardeberg, "Deep hyperspectral prior: Single-image denoising, inpainting, super-resolution," in *Proceedings of the IEEE International Conference on Computer Vision Workshops*, 2019, pp. 0–0.

[13] Gary Mataev, Peyman Milanfar, and Michael Elad, "Deepred: Deep image prior powered by red," in *Proceedings of the IEEE International Conference on Computer Vision Workshops*, 2019, pp. 0–0.

[14] Kary Ho, Andrew Gilbert, Hailin Jin, and John Collomosse, "Neural architecture search for deep image prior," *arXiv preprint arXiv:2001.04776*, 2020.

[15] José M Bioucas-Dias, Antonio Plaza, Nicolas Dobigeon, Mario Parente, Qian Du, Paul Gader, and Jocelyn Chanussot, "Hyperspectral unmixing overview: Geometrical, statistical, and sparse regression-based approaches," *IEEE journal of selected topics in applied earth observations and remote sensing*, vol. 5, no. 2, pp. 354–379, 2012.

[16] Sen Jia and Yuntao Qian, "Constrained nonnegative matrix factorization for hyperspectral unmixing," *IEEE Transactions on Geoscience and Remote Sensing*, vol. 47, no. 1, pp. 161–173, 2009.

[17] Fumihito Yasuma, Tomoo Mitsunaga, Daisuke Iso, and Shree K Nayar, "Generalized assorted pixel camera: postcapture control of resolution, dynamic range, and spectrum," *IEEE transactions on image processing*, vol. 19, no. 9, pp. 2241–2253, 2010.

[18] Bee Lim, Sanghyun Son, Heewon Kim, Seungjun Nah, and Kyoung Mu Lee, "Enhanced deep residual networks for single image super-resolution," in *Proceedings of the IEEE conference on computer vision and pattern recognition workshops*, 2017, pp. 136–144.

[19] Yulun Zhang, Kunpeng Li, Kai Li, Lichen Wang, Bineng Zhong, and Yun Fu, "Image super-resolution using very deep residual channel attention networks," in *Proceedings of the European conference on computer vision (ECCV)*, 2018, pp. 286–301.

[20] Tao Dai, Jianrui Cai, Yongbing Zhang, Shu-Tao Xia, and Lei Zhang, "Second-order attention network for single image super-resolution," in *Proceedings of the IEEE/CVF Conference on Computer Vision and Pattern Recognition*, 2019, pp. 11065–11074.

[21] Yong Li, Lei Zhang, Chen Dingl, Wei Wei, and Yanning Zhang, "Single hyperspectral image super-resolution with grouped deep recursive residual network," in *2018 IEEE Fourth International Conference on Multimedia Big Data (BigMM)*. IEEE, 2018, pp. 1–4.

[22] Diederik P Kingma and Jimmy Ba, "Adam: A method for stochastic optimization," *arXiv preprint arXiv:1412.6980*, 2014.

[23] Tatiana Gelvez and Henry Arguello, "Nonlocal low-rank abundance prior for compressive spectral image fusion," *IEEE Transactions on Geoscience and Remote Sensing*, vol. 59, no. 1, pp. 415–425, 2020.

[24] Tatiana Gelvez, Hoover Rueda, and Henry Arguello, "Joint sparse and low rank recovery algorithm for compressive hyperspectral imaging," *Applied Optics*, vol. 56, no. 24, pp. 6785–6795, 2017.